Volume 8 | Number 1 | 7 January 2016 | Pages 1–660

Nanoscale

www.rsc.org/nanoscale

ISSN 2040-3364

PAPER
Qian Wang et al.
TiC₂ a new two-dimensional sheet beyond MXenes

ROYAL SOCIETY OF CHEMISTRY

rsc.li/nanoscale

Superresolution Stimulated Raman Scattering Microscopy Using 2-ENZ Nano-Composites

Sergey S. Kharintsev[1]*, Anton V. Kharitonov[1], Alexander M. Alekseev[2,3] and Sergei G. Kazarian[4]

[1]Department of Optics and Nanophotonics, Institute of Physics, Kazan Federal University, Kremlevskaya, 16, Kazan, 420008, Russia

[2]National Laboratory Astana, Nazarbayev University, Kabanbay batyr Ave., 53, Astana, 01000, Kazakhstan

[3]National Research University "MIET", Moscow, Moscow, 124498, Russia

[4]Department of Chemical Engineering, Imperial College London, SW7 2AZ, United Kingdom

*To whom correspondence should be addressed. E-mail: (S.S.K.) Sergey.Kharintsev@kpfu.ru

ABSTRACT

Superlensing plays a crucial role in near- and far-field optical imaging with sub-wavelength resolution. One of the ways to expand optical bandwidth is surface plasmon resonances in layered metal-dielectric nanostructures. These resonances are commonly excited at a tunable single frequency. In this study, we propose the concept of a multimode far-field superlens comprising a titanium oxynitride (TiON) thin film, being a disordered metal-dielectric refractory nano-composite. These films exhibit a double epsilon-near-zero (2-ENZ) behavior near the percolation threshold and, therefore, favor super-coupling the incident laser light to surface plasmon resonances, not using such couplers as a prism, a grating etc.

We experimentally observe stimulated Raman gain emission from nano-structured TiON thin films exposed to low-power continuous-wave laser light. It is shown that super-resolution of $<\lambda/80$ (near-field) and $<\lambda/8$ (far-field) is achieved due to both the enhanced third-order optical nonlinearity and the multiplicative nature of four-wave mixing. The multimode tunable far-field superlens will impact emerging diffraction-free far-field optical microscopy, random Raman lasing on meta-atoms and broadband thermophotovoltaics.

KEYWORDS: nonlinear plasmonics, superresolution, leaky modes, antenna-enhanced stimulated Raman scattering, titanium oxynitride, double epsilon-near-zero material, refractory thin film

1. Introduction

Refractory plasmonics is rapidly emerging platform for alternative plasmonic materials able to enhance the light trapping over a wide range of frequencies.[1–4] They have found diverse applications in many interdisciplinary areas, including nonlinear optics,[5–7] nanolasing,[8,9] photovoltaics,[10,11] and superlensing.[12,13] The most popular class of underlying refractory materials is transition metal nitrides (TiN, ZrN, HfN, NbN, etc.).[14–16]

Titanium oxynitride (TiON) thin films, recently synthesized by Mihai and coworkers,[17] exhibit a tunable double epsilon-near-zero (2-ENZ) behavior in the visible and near-infrared regions. One should be noted that optical effects at ENZ wavelengths, such as supercoupling, enhanced directivity and bandwidth, light emission and trapping, giant nonlinearity etc. are to date the subject of intensive investigations.[18-22] Generally speaking, the synthesized TiON thin films comprise a mixture of TiN, TiO_x, and TiO_xN_y compounds, and represent refractory ceramics. Using the Maxwell-Garnett theory (MGT), the origin of this phenomenon can in a first approximation be understood by diluting nano-sized metallic inclusions of TiN within a TiO_2 host.[17] Near-field interactions between adjacent metallic inclusions can be further enhanced through delocalized surface plasmon-polaritons (SPPs) or leaky (quasi-bound)

modes (LMs) excitation.[23-25] Interparticle junctions behave as hot spots that are able to enhance electric fields as strongly as interatomic fields, and, thus, higher-order optical nonlinearities become possible on the nanoscale.[13] If the metamaterial of interest is a Raman-active medium then inelastically scattered Raman photons, down-shifted by the phonon frequency Ω, are generated. Strong internal electrical fields allow a confined Raman-active medium to support the beating between a SPP/LM pump and a localized Stokes signal and, thus, stimulated Raman scattering (SRS) occurs. It leads to the generation of a coherent wave of synchronized lattice vibrations that further exponentially enhances scattering into one of the overtones with frequencies $\omega_m = \omega_0 - m\Omega$ (ω_0 is a pump frequency, $m = 1, 2, \ldots$). The specific behavior of the 2-ENZ metamaterial in the vicinity of the zero points permits light to freely couple and/or decouple with the SPP/LM, not using such couplers as a prism, a grating, etc.[23]

In this paper, we report on LM-assisted stimulated Raman scattering from continuous and nano-structured TiON thin films exposed to continuous-wave (cw) laser light with the power of a few mW's. We demonstrate the superlensing effect[13,26,27] by showing a super-resolution of <10 nm and <100 nm in the near- and far-field regions, respectively. This effect is a recognition of the multiplicative nature of the SRS and the enhanced third-order optical nonlinearity. With the latter, we show below that the sub-wavelength resolution is achieved through the strong localization of the internal electric fields at Stokes frequencies that sustains the propagation of quasi-bound slow modes inside lossy media with the increased group refractive index.

2. Results and discussions

One of the ways to overcome the Abbe's diffraction limit is the "perfect" lens invented by Sir John Pendry.[28] However, its practical implementation is still limited by the lack of optical magnetism for the underlying negative index metamaterial.[13] Later, Pendry proposed a

simplified version of the superlens, known as a near-field superlens (NFSL), that relies on a

single negative mechanism only: $\varepsilon < 0$ and $\mu > 0$.[28] Such the NFSL consists of a metal

(plasmonic) slab sandwiched between two dielectric layers, as schematically shown in Fig. 1

(a). The practical implementations of the superlens were demonstrated by different research

groups.[29-32] As seen from this figure, the NFSL operates at a single frequency defined from

the Fröhlich condition, Eq. (1). This greatly restricts its application in practice. Shalaev *et*

al[13,33] succeeded to circumvent this limitation by considering random metal-dielectric

composite as
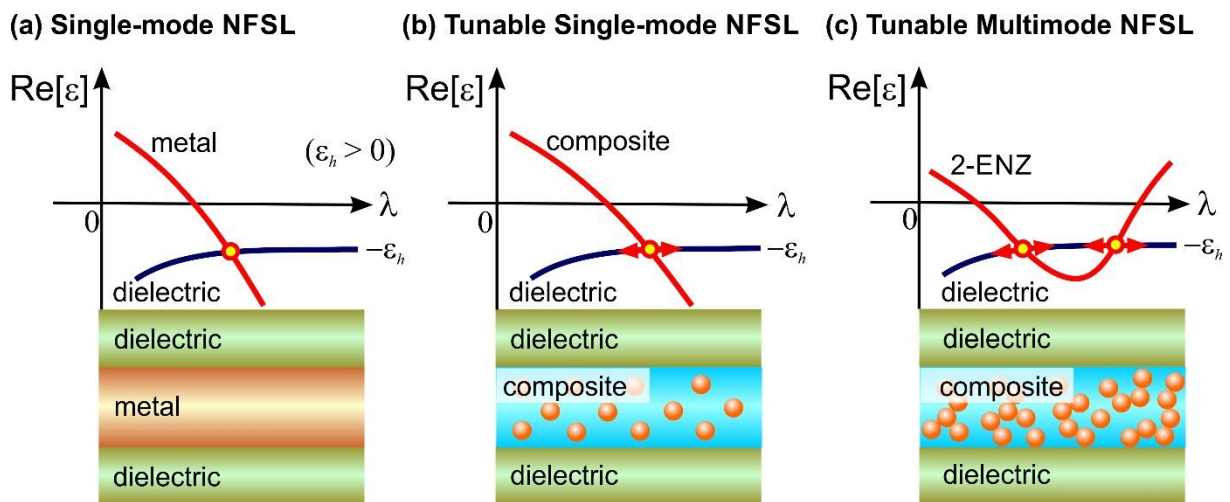
Figure 1. Sketch of a single-mode NFSL (a), a tunable single-mode NSFL (b) and a tunable

multi-frequency NSFL (c).

the NFSL material. Fig. 1 (b) shows a case where the metal slab is substituted by the d-

dimensional composite. This composite with the effective electrical permittivity $\varepsilon_{\mathrm{eff}}$ is

sandwiched between two dielectric host layers with the permittivity ε_h. Without going into

the details of the intrinsic structure of the composite, the condition to excite SPP/LM reads

as[23]

$$Re[\varepsilon_{\mathrm{eff}}(\omega, d)] = -\varepsilon_h, \qquad (1)$$

Despite the fact that the composite-based NFSL functions as an single-mode lens, this allows us to adjust the operational frequency within the desirable range.[13] For example, the tunable NFSL pushes the operational frequency outside the plasmon absorption band and, thus, decreases significant losses to deliver as much information as possible into the far-field.

In attempts to create a multi-frequency tunable far-field superlens we used disordered metal-dielectric composite that reveals a double epsilon-near-zero (2-ENZ) behavior in the vicinity of the percolation threshold, as shown in Fig. 1 (c). By analogy to the single-mode NFSL, two singular points are arranged owing to the intrinsic structure of the composite. Using the 2-ENZ metamaterial, we can potentially achieve the multi-frequency super-resolution through stimulated Raman scattering by detecting the higher-order overtones.
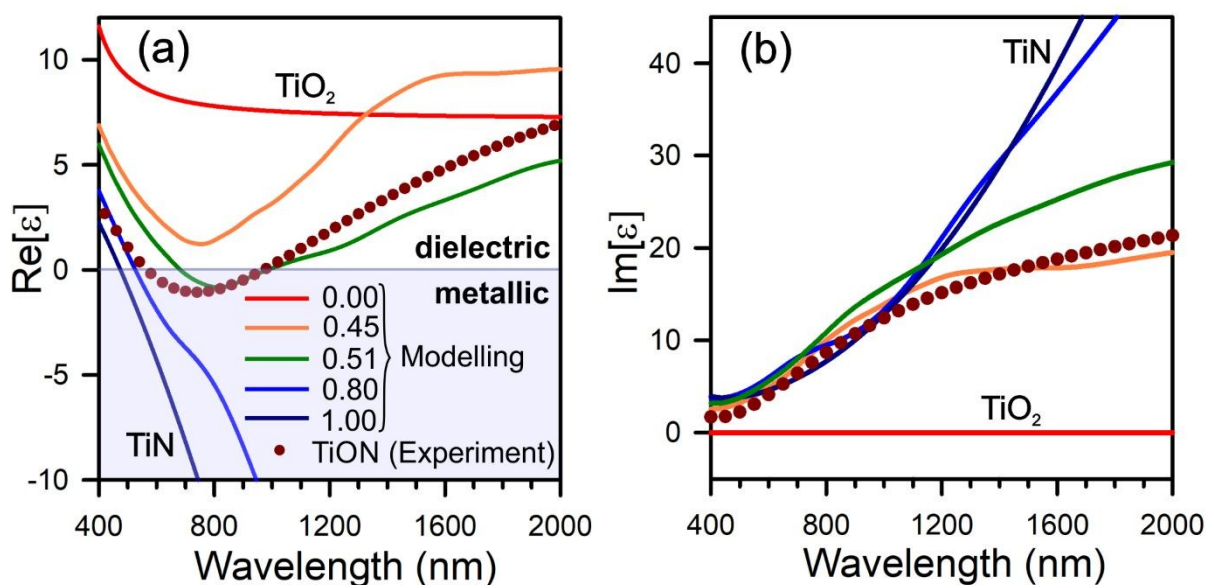
Figure 2. FDTD calculated real part (a) and imaginary part (b) of effective permittivity of a TiN/TiO$_2$ composite with different volume filling factor, f, vs wavelength (solid curves) and their experimental counterparts for a TiON thin film (dotted curve). The limiting cases when $f = 0$ and $f = 1$ correspond to TiO$_2$ and TiN, respectively.

In our study we used a 50 nm TiON film prepared by using magnetron sputtering under controllable pressure of residual oxygen in the background vacuum between 5 and 20 nTorr at

room temperature.[17] The appearance of 2-ENZ frequency is related to a heterogeneous mixture of metallic TiN and dielectric TiO_xN_y/TiO_x constituents. This problem can be simplified by considering the metamaterial as a nano-composite consisting of TiN and TiO_2.[17] The MGT gives a clear interpretation of the 2-ENZ effect provided that metallic inclusions are out of direct contact with each other. However, this approach is not suitable for the composite nearby the percolation threshold when the metallic inclusions form dc electrical conducting pathways. The light entering into on the TiN/TiO_2 composite film excites localized surface plasmons according to the Fröhlich condition:[23] $Re[\varepsilon_{TiN}(\omega)] = -[(l+1)/l]\varepsilon_{TiO_2}$ (where l is an order of a surface plasmon mode). Near-field coupling between touching and/or closely spaced metallic nanoparticles generates longitudinal and transverse plasmon modes that travel along these nanoparticle chains. These microscopic models have been the subject of intensive studies.[24,25]

As a result, the effective permittivity of a TiN/TiO_2 mixture with a volume filling factor f, so that its percentage composition is defined as $TiN/TiO_2 = f\,TiN + (1-f)TiO_2$ ($0 \leq f \leq 1$), was numerically calculated through a S-parameter retrieval using finite difference time domain (FDTD) method (FDTD Lumerical software).[34,35] Simulations of the real and imaginary parts of the effective permittivity are given for various f in Fig. 2 (a) and (b). These with $f = 0.51$ and $f = 0.45$ are satisfactorily fitted to the experimental curves measured with spectroscopic ellipsometry (UVISEL 2 Horiba). The real part of the permittivity intersects the zero line twice. The cross-over frequencies, ω_c ($Re[\varepsilon_{eff}] = 0$) are equal to $\omega_c' = 1.27\,eV$ and $\omega_c'' = 2.38\,eV$. They lay on the SPP and LM branches of the S-shaped dispersion curve, respectively, and limit a region colored green, as shown in Fig. 3 (b). As follows from Fig. 2 (a) and Fig. (b) the width of the LM, defined as $Im[\varepsilon_{eff}]$ when $Re[\varepsilon_{eff}] = 0$, is narrower than that of the SPP.[15] Within the visible region, these widths are

almost independent of f. On the other hand, this parameter is driven by magnetron sputtering

conditions and plays a pivotal role to exhibit the 2-ENZ behavior.
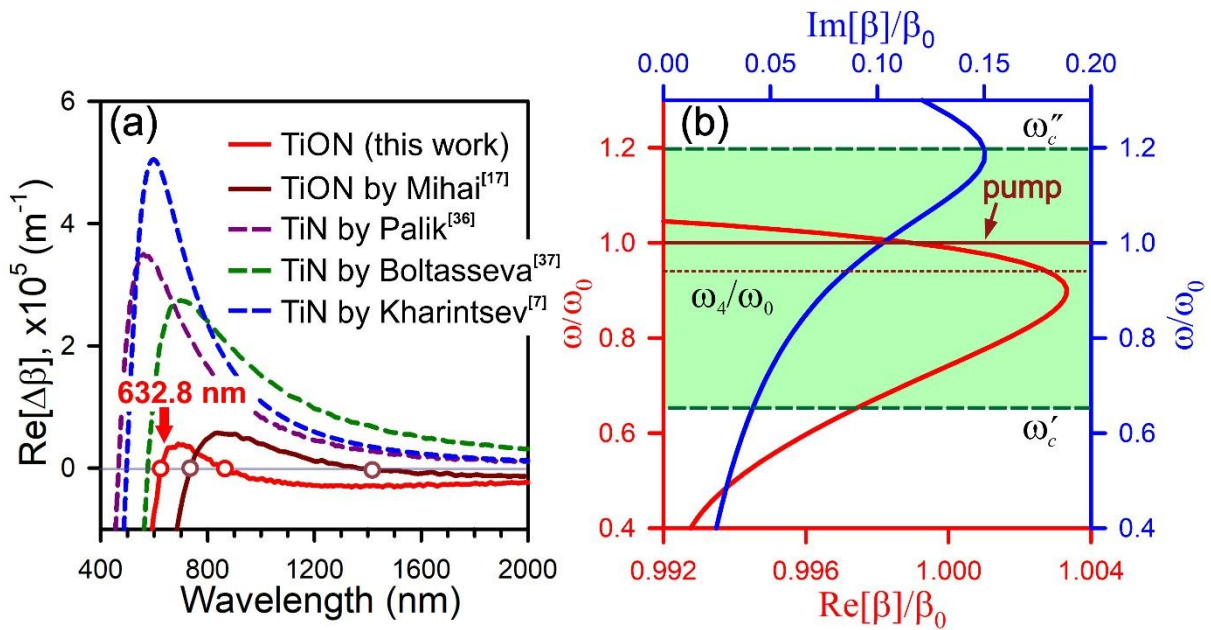
Figure 3. (a) A dependence of $\mathrm{Re}[\Delta\beta]$ on wavelength for TiN and TiON thin films

synthesized by different research groups, (b) the real (red curve) and imaginary (blue curve)

parts of the dispersion curve for the TiON (this work) thin film. Solid and dotted horizontal

lines highlight frequencies for the pump ω_0 and the 4th Stokes harmonics. A green bar

indicates the energy band between the cross-over frequencies $\omega_c' = 1.27\,\mathrm{eV}$ and

$\omega_c'' = 2.38\,\mathrm{eV}$.

In order to demonstrate the specific feature of this material we plot the difference between the

SPP/LM and light propagation constants, $\Delta\beta = \beta - \beta_0$, (where $\beta \equiv k_x = k_0\sqrt{\varepsilon_{\mathrm{eff}}/(\varepsilon_{\mathrm{eff}}+1)}$,

$\beta_0 = k_0$, k_0 is a wavevector of light in vacuum) vs wavelength (Fig. 3 (a)). Such approach

allows one to magnify the small but crucial deviation from the linear dispersion relation of air,

$\omega = c\beta_0$. It is important to note that here we utilize the effective medium theory.[13] In other

words, the composite film represents itself a continuous medium with the effective

permittivity $\varepsilon_{\mathrm{eff}}$. Compared to conventional TiN thin films, previously synthesized by

different groups,[7,36,37] the dispersion curve of the 2-ENZ metamaterial is slightly deviated from the light line. It means that the SPP/LMs are easily excited nearby the cross-over frequencies ω_c. Small values $\Delta\beta$ permit light at $\min(\omega_c) \leq \omega \leq \max(\omega_c)$ to get coupled/decoupled with the SPP/LMs.

In our experiments we excited the leaky modes in the TiON thin film using the cw laser light with a wavelength of 632.8 nm ($\omega_0 = 1.96$ eV). As seen from Fig. 3 (b) this wavelength (horizontal solid curve) falls into the leaky mode branch of the dispersion curve. A green region shows the energy band between the cross-over frequencies where the composite film meets the metallic behavior. It is important to notice that the leaky mode is excited outside of the absorption peak at $\omega/\omega_0 = 1.18$ (blue curve in Fig. 3 (b)). For clarity, we indicated the 4th Stokes overtone at the frequency $\omega_4 = \omega_0 - 4\Omega$ ($\Omega = 240$ cm^{-1}). Thus, the first four overtones lay on the very edge of the 'plasmon bandgap'. Fig. 3 (b) shows that the pumping leaky mode is generated within the near-zero refractive index medium $n_{\text{eff}} = \sqrt{\varepsilon_{\text{eff}}} < 1$.
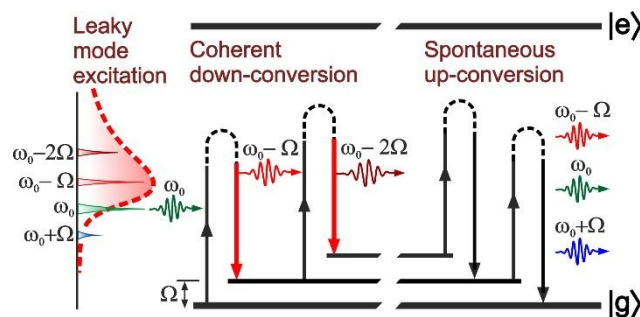
Figure 4. Schematic energy diagram of coherent stimulated Raman gain emission enhanced by leaky plasmon mode excitation and spontaneous up-conversion mechanism.

It is well-established that SPP-assisted stimulated Raman scattering may occur in confined Raman-active media.[7] The intensity of the localized Stokes wave $I_m(L)$, as a function of the distance L, experiences an exponential growth at the down-shifted frequency ω_m: $I_m(L) = I_m(0)\exp[\chi_R(\omega_m)I_0 L]$. Clearly, the strength of the optical amplification is

provided by maximizing the product $\chi_R(\omega_m)I_0L$. Since we deal with the confined medium, $L \rightarrow 0$, and the low-intensity pump I_0 (a few $\mathrm{mW/cm^2}$), the SRS performance may be improved by enhancing the Raman gain factor $\chi_R(\omega_m)$ only. The energy exchange between the pump and the Stokes components can be enhanced by surface plasmon resonances, as shown in Fig. 4. It means that if one of the Stokes waves spectrally matches the resonance of the LM, its amplitude greatly enhances and becomes comparable with that of the pump. As a result, we observe a coherent down-conversion or stimulated Raman gain emission. Since the anti-Stokes wave is non-resonant with the LM, stimulated Raman loss emission does not occur and, therefore, the up-conversion is spontaneous.

In the SRS regime all four waves ($\omega_m = \omega_0 + \omega_m - \omega_0$) become enhanced. Thus, the third-order Raman susceptibility changes as

$$\chi_R^{(3)}(\omega_m; \omega_0, -\omega_0, \omega_m) \rightarrow g_0^2 g_m^2 \, \chi_R^{(3)}(\omega_m; \omega_0, -\omega_0, \omega_m)\,, \tag{2}$$

where g_0 and g_m are the local field-enhancement factors for the pump and the Stokes signal, respectively. With that, the Raman gain factor $\chi_R(\omega_m)$ reads as:

$$\chi_R(\omega_m) = -\frac{3\omega_m}{n_m n_0 \varepsilon_0 c^2} \, g_0^2 g_m^2 \, \mathrm{Im}[\chi_R^{(3)}]\,, \tag{3}$$

where $n_0 = n(\omega_0)$ are $n_m = n(\omega_m)$ are the group refractive indexes for the pump and the Stokes wave, c is the speed of light in vacuum. Compared to the approach considered in Ref.[7], both the field enhancements of the pump and the Stokes wave are taken into account in Eq. (3). The real part of $\chi_R^{(3)}$ contributes into the accumulated Raman phase shift $\Delta\phi_R$ for the Stokes wave and it corresponds to the Kerr optical nonlinearity. As follows from Eq. (3) a link between the group and effective refractive index, n_m and n_{eff}, at the Raman shift ω_m is expressed by the following relationship

$$g_m = \sqrt{\frac{n_m}{n_{\mathrm{eff}}}}\,. \tag{4}$$

In conventional nonlinear optics, the characteristic length for significant four-wave mixing is estimated to be $\Lambda \sim \lambda |E_a|/|E_0|$, where λ is a wavelength of the incident light, $\boldsymbol{E}_0$ is the incident electrical field. Let us assume that $\lambda = 633\,\text{nm}$, $\boldsymbol{E}_0 = 3 \times 10^4\,\text{V/cm}$ (it corresponds to the intensity of $\sim \text{MW/cm}^2$) and $\boldsymbol{E}_a = 3 \times 10^8\,\text{V/cm}$ then $\Lambda = 0.6\,\text{cm}$.[38] Naturally, a reasonable question arises – whether the nonlinear effects can appear on the sub-wavelength scale? To answer this question, the above mentioned criterion must be modified as follows: $\Lambda^* \sim \rho |E_a|/|E_{\text{loc}}| = (\rho/g_0^4)(|E_a|/|E_0|)$ (where ρ is a light localization). By setting $g_0 = 10$ and $\rho = 25\,\text{nm}$ we derive the following estimate of $\Lambda^* \sim 25\,\text{nm}$. For larger g_0 this distance can potentially reach several nm's or less. Thus, the SRS can be generated on the nanoscale.

Fig. 5 (a) and (b) show a surface AFM topography and dc electrical current map of the TiON thin film. We observe the irregular surface structure dotted with TiON platelets of 10 nm in diameter, as follows from Fig. 5 (a). Bright spots on the dc conductivity image indicate the shaping of continuous conducting chains inside the film. Such worm-like chains within the film can potentially result in the artificial optical magnetism in the TiON film. Observable gaps between nanoparticles on the film surface are caused by topography artifacts or non-conducting oxide particles. Once the volume filling factor f reaches the critical value $f_c = 1/d$ (or the percolation threshold), the interparticle gaps enhance the internal electrical fields as highly as the interatomic electrical field of $3 \times 10^8\,\text{V/cm}$.[13]
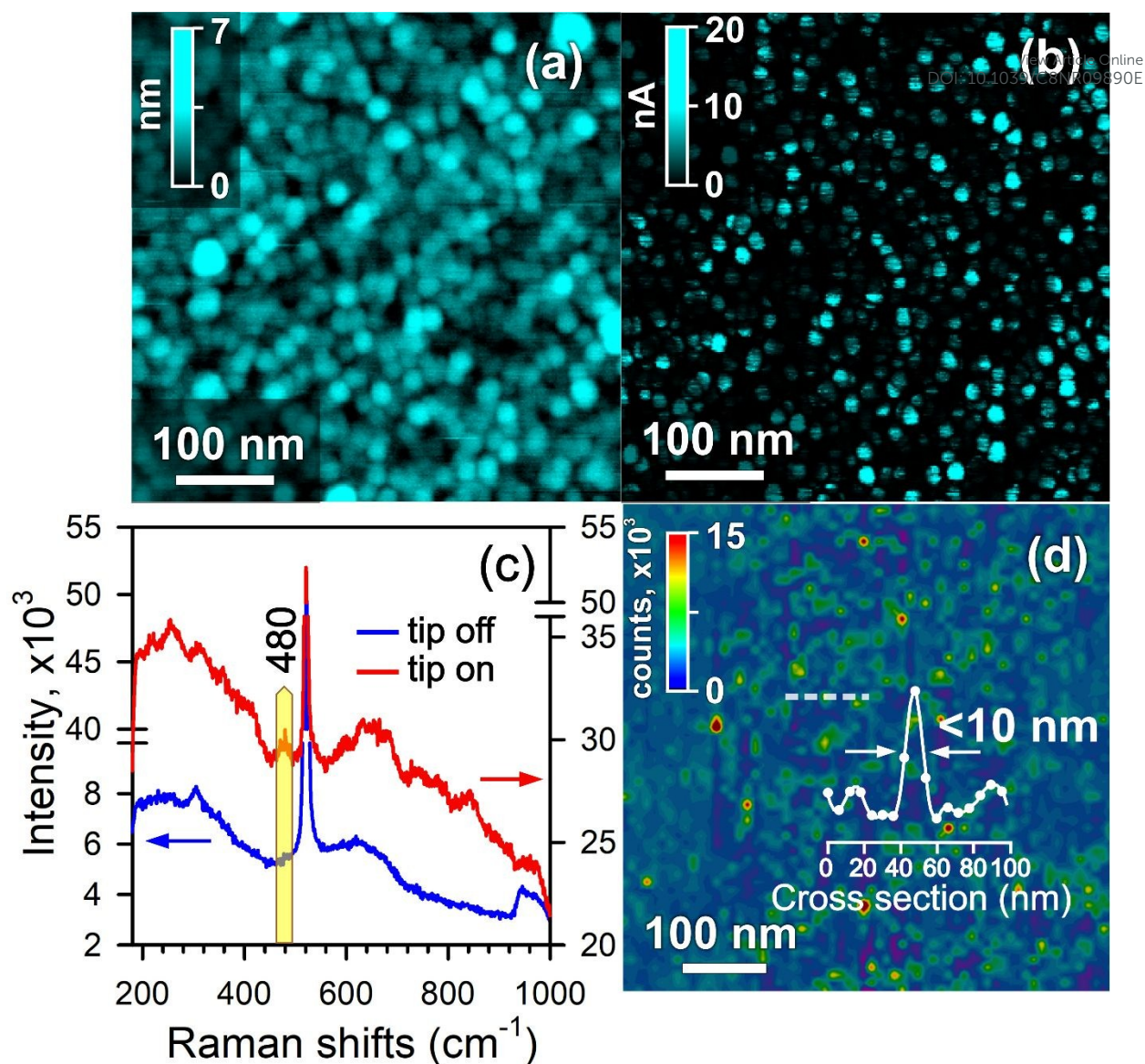
Figure 5. (a) AFM topography and (b) dc electrical current map of the 50 nm thick TiON film. (c) Far-field (tip off) and near-field (tip on) Raman spectra, and (d) TERS mapping at 480 cm^{-1} of the same film.

A chemical analysis of the TiON thin film is performed with far- and near-field Raman spectroscopy and nanoscopy, as demonstrated in Fig. 5 (c) and (d). All spectroscopic measurements were performed with a SPM-equipped confocal Raman spectrometer NTEGRA SPECTRA (NT-MDT). In TERS experiments we used a cone-shaped gold tip with a curvature radius of 25 nm. The raster scanned tip was exposed to a 632.8 nm linearly-polarized laser beam focused with a 100x objective (N.A.=0.7) in epi-configuration.

As shown in Fig. 5 (c), the far-field Raman spectrum (blue curve) exhibits a broad band of 580-700 cm^{-1}, that is a prerequisite for assigning to multi-phase TiO$_2$.[39] This hypothesis is verified by capturing a TERS spectrum (red curve) of the TiON thin film. With that, the band is decomposed into the four elementary peaks attributed to mixed crystalline phases of TiO$_2$ – (a) rutile at 600 cm^{-1} and 630 cm^{-1}, and (b) anatase at 655 cm^{-1} and 680 cm^{-1}.[40,41] It is important to notice that the observable peaks are buried within a broadband background assigned to the amorphous phase of TiO$_2$. The peaks at 254 and 360 cm^{-1} indicate the presence of brookite.[42] Also, the TERS spectrum shows the first- and second-order Raman spectral features of TiN at 240 and 460 cm^{-1}. Thus, the synthesized TiON thin films contain mixtures of metallic TiN and dielectric multi-phase TiO$_2$ consisting of varying amorphous, anatase, rutile, and brookite constituents. Our experimental data support the assumption, made by Mihai *et al*,[17] that the TiON thin film can be represented as a mixture of TiN/TiO$_2$ to get insight into the 2-ENZ behavior using the MGT.

The most important finding is the occurrence of the band at 480 cm^{-1} that is assigned to the second overtone of the SRS. Unlike the nano-patterned TiN thin films,[7] the SRS generation is observed for the continuous TiON thin films. The underlying effect is caused by chaining TiN particles that serve as optical antennas inside the dielectric matrix. The full width at half height (FWHH) of the SRS band is equal to 16 cm^{-1} and 50 cm^{-1} for TiON and TiN,[7] respectively, under the same conditions. The reason can be attributed to a stronger electrical field between the tip apex and the TiN platelet due to SRS assisted plasmon gap mode excitation. In particular, this explains the origin of a sub-tip spatial resolution of <10 nm (or λ/80), as shown in Fig. 5 (d). A spatial resolution is found from a cross section along a white dashed line. Since all spectroscopic spots are similar to each other, we suppose that real sizes of the TiN platelets can be even less. By analogy with dc conductivity, the SRS spots on the TERS map at 480 cm^{-1} reflect the presence of Raman-active TiN particle chains. Thus, the

electrical and spectroscopic properties of the TiON thin films are well consistent with each other.

Perhaps most intriguing feature of the 2-ENZ metamaterial is its capability to far-field superlensing.[33,43] For this purpose, we fabricated a 100x100 nm^2 square antenna on the TiON thin film with focused ion beam (FIB) milling, as shown in Fig. 6 (a). It is worth noticing that rounded corners of the antenna inevitably occur due to both the non-uniform distribution of the ion beam intensity and the re-deposition of the structure material itself while FIB milling.[44]   Far-field Raman spectra taken at the film surface (blue curve) and the antenna (red curve) are given in Fig. 6 (b). Compared to the TERS spectrum (Fig. 5 (c)), we observe the modest intensity enhancement of all spectral bands except the SRS band at 480 cm^{-1}. This is stipulated by the larger size of the
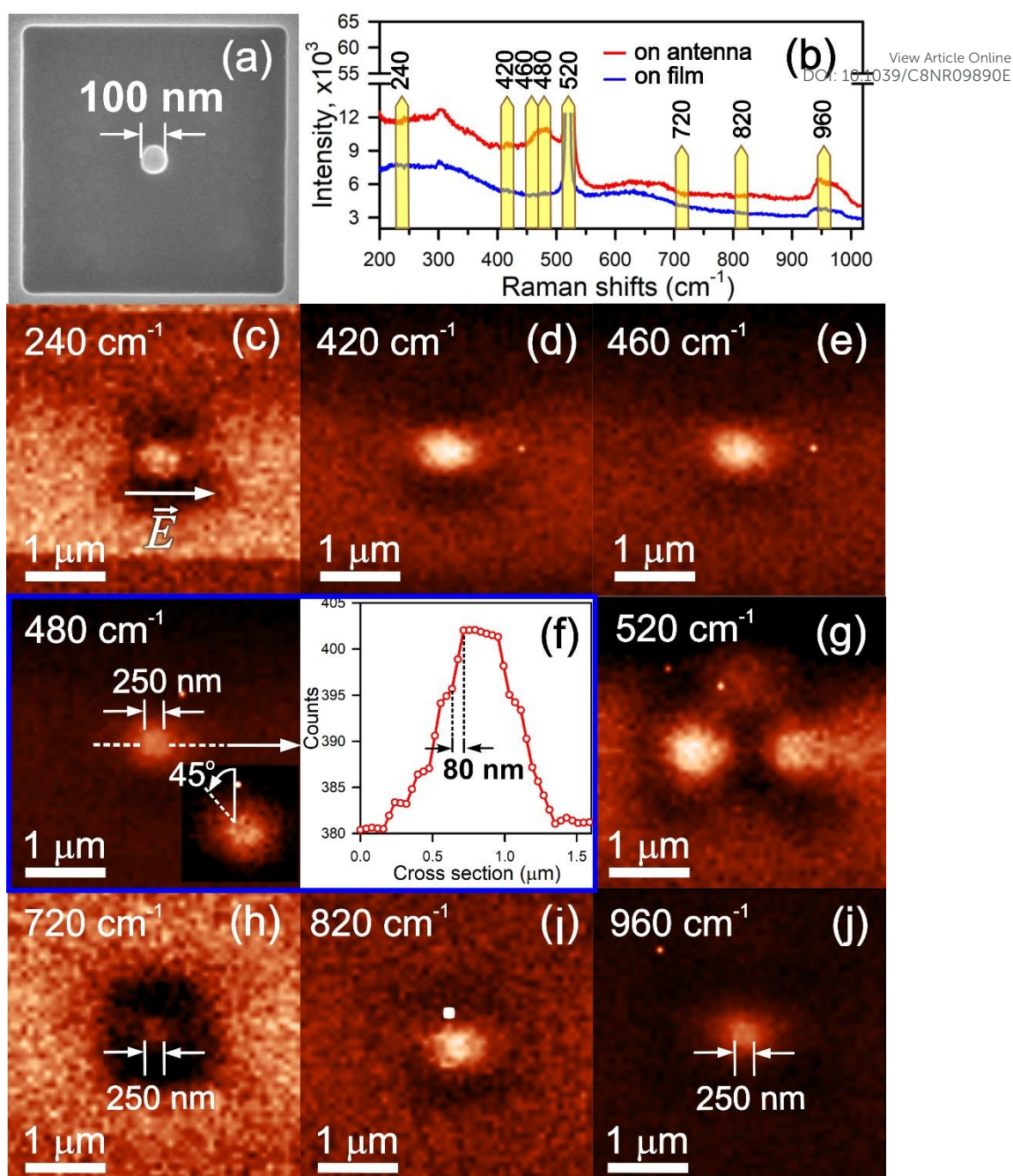
Figure 6. (a) SEM image of a planar square TiON antenna with the size of 100 nm, (b) far-field Raman spectra captured on both the film and the antenna, (c)-(j) far-field Raman maps of the antenna registered at different vibrational modes, as indicated in Fig. 6 (b). The inset in Fig. 6 (f) shows the Raman map at 480 cm^{-1} of the antenna rotated by 45 degrees angle.

focal spot, that is on the order of λ, and, therefore, the lower radiative resistance proportional to $\sim (a/\lambda)^2$ (a is the length of the square antenna). Unlike the tip-sample cavity, the larger extent of the antenna provides a better SRS performance. Importantly, the FWHH of the SRS

band is much broader than that of the TERS band at 480 cm^{-1}. The same has been earlier observed for the planar TiN antennas.[7] The origin of the anomalous FWHH of the SRS response from confined Raman-active media is still under debate.

Figs 6 (c-j) show far-field Raman maps at the wavenumbers indicated by the yellow bars in Fig. 6 (b). A direction of the electric field of the impinging linearly polarized light wave is indicated with an arrow in Fig. 6 (c). Using the first- and second-order Raman peaks of TiN at 240 and 460 cm^{-1}, we observe the diffraction-limited images of the planar square antenna. The same appears at the Raman shift of 420 cm^{-1}. The antenna of interest is well resolved when using the second overtone of the SRS at 480 cm^{-1} as depicted in Fig. 6 (f). It is important to note that we observe a perfect square rather than a circle as shown in Fig. 6 (a). This is affected by the pixelization of the antenna image on the EMCCD detector. The inset in Fig. 6 (f) testes the hypothesis by rotating the square antenna by 45 degrees angle. We clearly see that the antenna shape remains unchanged, whereas the image of the antenna edge is degraded. The cross section along a dashed straight line demonstrates the spatial resolution of ca. 80 nm. Indeed, the observable extended structure has the size of 250 nm, but the original size should be 100 nm. Taking two edge-like sides of the antenna into account, we conclude that the spatial resolution of ca. 80 nm (or $\lambda/8$) is achieved. Fig. 6 (g) demonstrates a Raman map at 520 cm^{-1} assigning to p-doped Si (100). Unlike the TiN bands, a two-lobe pattern towards the light polarization is observed. To verify the hypothesis concerning the far-field super-resolution we have captured the far-field Raman image at 820 cm^{-1} (see Fig. 6(i)). As seen from this figure the blurred image of the antenna occurs again. Using the higher-order overtones of the SRS at 720 and 960 cm^{-1} we see the well-resolved geometry of the square antenna far beyond the diffraction limit, as observed at the second overtone of 480 cm^{-1}. In the former case, we meet a lower signal-to-noise ratio and, therefore, the SRS contrast is negligible. Whereas the latter case demonstrates the SRS overtone fully overlapping with the second-order Raman peak of Si coming from a substrate. Despite the fact, the 4th overtone

provides the higher SRS contrast as well. Interestingly, a much better performance in the spatial resolution is achieved for the SRS overtones. The physical origin of this phenomenon can be clarified by the increased group refractive index due to the local field enhancement factor, Eq. (4). In other words, the enhanced leaky slow-mode propagates along conducting nanoparticles chains within near-zero refractive index media. As a result, the Airy function $PSF(\rho,\theta)$, inevitably becomes narrower

$$PSF(\rho,\theta) = \left| J_1\left(kn_{\text{eff}}\, g_m^2\, \rho \sin(\theta)/2\right) \big/ kn_{\text{eff}}\, g_m^2\, \rho \sin(\theta)/4 \right|^2, \tag{5}$$

where $J_1(x)$ is a Bessel function of the first kind. Thus, as follows from Eq. (5), the spatial resolution is eventually determined by the local field-enhancement factor g_m. It is important to note that this result is valid for the Stokes components $\omega_m = \omega_0 - m\Omega$ only. It means that in the total scattered light we can observe the super-resolution effect at the anharmonicity-free overtones.

It may be realized that the whole antenna surface radiates more or less uniformly and this is not localized to the edges of the sample, as has been observed with the planar TiN antenna.[7] This follows the slight deviation of the dispersion curve of the 2-ENZ metamaterial from the light line and the presence of the intrinsic roughness of the antenna surface. Finally, we can conclude that the SRS provides the super-resolution of ca. 80 nm in the far-field, in our case, $\sim \lambda/8$. Previously, the similar result, $\sim \lambda/6$, was obtained through coherent anti-Stokes Raman scattering by using a Toraldo-style pupil phase filter.[26]
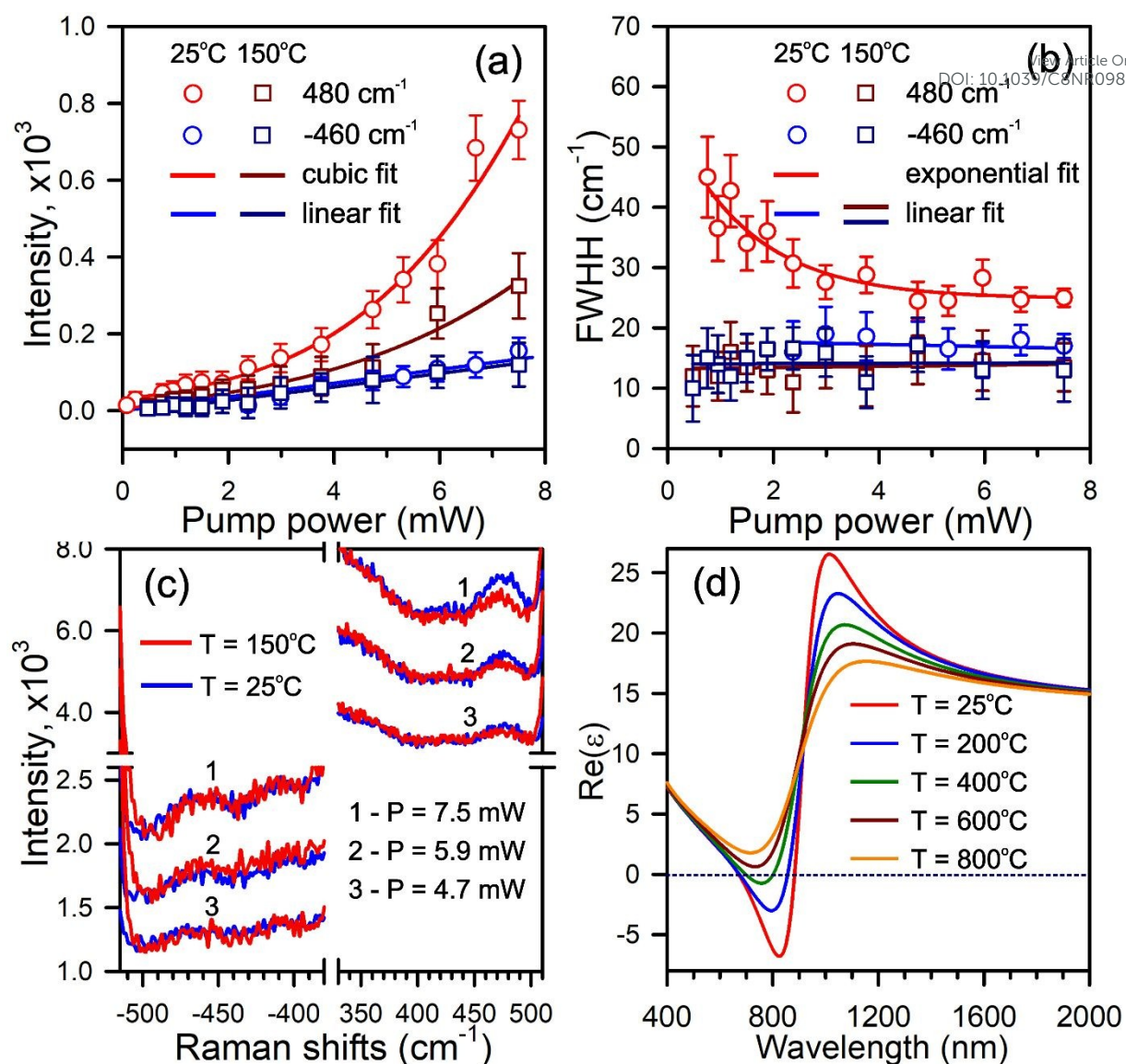
Figure 7. (a) Raman intensity and (b) full width at half height (FWHH) vs pump power for the SRS signal (480 cm^{-1}) and the 2nd overtone of anti-Stokes wave (-460 cm^{-1}) at different temperatures (solid curves stand for fitting), (c) anti-Stokes and Stokes Raman spectra at different temperatures for various pump power, (d) simulation of the real part of effective permittivity of a TiN/TiO$_2$ composite ($f = 0.3$) vs wavelength at various temperatures using MGT.

Another important contribution into the resolution improvement is the multiplicative nature of the SRS. It is well established that the third-order nonlinear effects are recognized by (1) the cubic behavior of the SRS intensity I_m vs the pump power I_0:

$$I_m = aI_0 + bI_0^3, \qquad (6)$$

where a and b are constants for spontaneous and coherent contributions, respectively, and, as a result, (2) the decrease of the FWHH with the pump power, as shown in Fig. 7 (a) and (b). We consider the nonlinear Stokes component at 480 cm^{-1} and the second-order anti-Stokes component of TiN at -460 cm^{-1} at room temperature of 25°C and elevated temperature of 150°C.

The experimental data for the 480 cm^{-1} band were fitted with Eq. (6) for both the temperatures with correlation coefficients of 0.998 and 0.994, respectively. A ratio of the spontaneous and coherent contributions is estimated to be $a/b = 16$ and $a/b = 40$. It is important to notice that photo-induced heating of the tip and/or antenna is not taken into account in our study. At the same time, the anti-Stokes components exhibit a linear behavior with the increase of the pump power. Decreasing the FWHH with the pump power does not lead into the expected threshold of around 16 cm^{-1} (Fig. 7 (b)). This is likely linked to the overlapping of the 460 and 480 cm^{-1} bands. Besides, an error of the FWHH becomes larger at the lower pump power. As seen from Fig. 7 (c), no SRS signal occurs at the anti-Stokes shift of -480 cm^{-1}, whereas, the second overtone of TiN is observed at both the Raman shifts of -460 and 460 cm^{-1}.

Figs. 7 (a)-(c) indicate the mitigation of the SRS effect with increasing temperature. To deeper understand this effect, let us consider the disordered TiN/TiO$_2$ composite with the volume filling factor below the percolation threshold, $f = 0.3$, and $d = 2$. Under these conditions, we can model the temperature-dependent effective permittivity $\varepsilon_{\text{eff}}(T)$ of the composite using the MGT, namely:

$$\left(\varepsilon_{\text{eff}}(T) - \varepsilon_{\text{TiO}_2}\right)\big/\left(\varepsilon_{\text{eff}}(T) + \varepsilon_{\text{TiO}_2}\right) = f\left(\varepsilon_{\text{TiN}}(T) - \varepsilon_{\text{TiO}_2}\right)\big/\left(\varepsilon_{\text{TiN}}(T) + \varepsilon_{\text{TiO}_2}\right). \qquad (7)$$

For simplicity, we neglect a temperature dependence of $\varepsilon_{\text{TiO}_2}$ and use tabulated data from Palik.[36] The temperature-dependent permittivity data $\varepsilon_{\text{TiN}}(T)$ were taken from Shalaev's paper.[45] With these, Fig. 7 (d) shows the real part of $\varepsilon_{\text{eff}}(T)$ at different temperatures. We see

that the minima peak position of the band increases with increasing temperature and, eventually, the composite reveals the dielectric behavior over the whole spectral range. Physically, this is linked to the temperature behavior of the volume plasma frequency ω_p driven with the electron density $n_e(T)$ and the effective mass of electron $m_e(T)$.[46,47] The imaginary part of $\varepsilon_{eff}(T)$ is affected by the electron-phonon scattering.[45]

3. Conclusion

In summary, we have demonstrated a birth of the SRS signal within the continuous and nanostructured TiON thin films exposed to the low-power continuous-wave laser light. The TiON thin films allow surface plasmon resonances to be easily excited at the ENZ wavelengths. The SPP/LMs sustain the generation of a coherent wave of synchronized lattice vibrations in conducting nanoparticle chains embedded within the dielectric host. Due to the enhanced internal electric fields at the Stokes overtones, the propagation of the leaky modes with a slowed group velocity may occur in the lossy medium. It means that this wave runs inside the medium with the increased group refractive index. This leads to the superlensing effect on certain frequencies in both the near-field ($<\lambda/80$) and the far-field ($<\lambda/8$) zones. Importantly, a PSF constriction can potentially be used for probing a local field enhancement factor (see Eq. 5). Also, we believe that our findings will benefit far-field diffraction-free optical imaging, random Raman lasing on meta-atoms and broadband thermophotovoltaics.

METHODS

Scanning probe microscopy

AFM measurements were performed using SPM Smart1000 (AIST-NT) equipped by Pt-coated probe CSG10/Pt (NT-MDT). The surface dc conductivity was probed in contact mode by applying voltage to the sample. A distance between the AFM cantilever, referred to

Nanoscale Accepted Manuscript

as a working electrode, and a counter electrode connected to upper surface was about 2 mm.

Tip-sample force was typically in the range of 10-15 nN during measurements.

Tip fabrication

Gold tips for TERS measurements were fabricated from a 100 μm gold wire (purity: 99.99%, Goodfellow) immersed in a mixture of fuming hydrochloric acid (HCl, 37%) and ethanol [C_2H_5OH, 96%] in a volume proportion of 1:1, using adaptive dc-pulsed electrochemical etching with a self-tunable duty cycle and working potentials of V_b = 1.5 V and V_{up} = 1.9 V.[48] On achieving the current cutoff event, the tips were safely retracted from the solution surface with a piezo-manipulator and were immediately rinsed with distilled water and dried with nitrogen. Curvature radii of the gold tips were estimated to be within the range of 20-30 nm. Prepared gold tips were under mechanical load to become bent and glued to a conductive long tab of a horizontally oriented tuning fork TF103_NTF (NT-MDT) operating at a resonance frequency of 192 kHz. Approaching the gold tip to the sample was safely performed with the help of a normal force feedback scheme at a setpoint value as small as 95%

Raman spectroscopy and nanoscopy

Far-field and near-field Raman spectra and mappings were captured with a multi-purpose analytical instrument NTEGRA SPECTRA™ (NT-MDT Spectrum Instruments) in epi-configuration. This represents a confocal Raman spectrometer equipped with a scanning probe microscope. The spectrometer was wavelength calibrated with a silicon wafer by registering a first-order Raman band centered at 520 cm^{-1}. A sensitivity of the spectrometer was as high as ca. 2500 photon counts per 0.1 s provided that we used a 100×objective (N.A.=0.7), an exit slit of 100 μm and a linearly polarized light with the wavelength of 632.8

nm and the power at the sample of 5 mW. No signal amplification regimes of a Newton EMCCD camera (ANDOR, Ireland) was applied.

A sample of interest was exposed to a laser light with the wavelength of 632.8 nm and the intensity of 1 kW/cm^2. The tip that performs quasi vertical oscillations at the distance of 2-3 nm above the sample. A signature of the surface localized plasmon based field enhancement beneath the apex gold tip was the rotation of a two-lobe Rayleigh scattering pattern at the focal plane when turning the linear polarization direction. 128x128 pixel TERS maps were raster scanned with a step of 50 nm and an exposure time per pixel of 0.1 s and were finally collected with the EMCCD camera cooled down to -80 ℃. Far- and near-field Raman spectra within the range of 200-2000 cm^{-1} were registered with spectral resolution of 3 cm^{-1} using a 600 grooves/mm grating.

Corresponding Author

*To whom correspondence should be addressed. E-mail: (S.S.K.) Sergey.Kharintsev@kpfu.ru

ACKNOWLEDGEMENT

NOTES AND REFERENCES

Nanoscale Accepted Manuscript

[1]   U. Guler, A. Boltasseva and V. M. Shalaev, *Science*, 2014, **344**, 263–264.

[2]   G. Albrecht, M. Ubl, S. Kaiser, H. Giessen and M. Hentschel, *ACS Photonics*, 2018, **5**, 1058–1067.

[3]   C. Metaxa, S. Kassavetis, J. F. Pierson, D. Gall and P. Patsalas, *ACS Appl. Mater. Inter.,* 2017, **9**, 10825–10834.

[4]   S. M. Choudhury, D. Wang, K. Chaudhuri, C. DeVault, A. V. Kildishev, A. Boltasseva and V. M. Shalaev, *Nanophotonics,* 2018, **7**, 959–987.

[5]   R. Sato, S. Ishii, T. Nagao, M. Naito and Y. Takeda, *ACS Photonics,* 2018, **5**, 3452–3458.

[6]   X. L. Wen, G. Y. Li, C. Y. Gu, J. X. Zhao, S. J. Wang, C. P. Jiang, S. Palomba, C. M. de Sterke and Q. H. Xiong, *ACS Photonics,* 2018, **5**, 2087–2093.

[7]   S. S. Kharintsev, A. V. Kharitonov, S. K. Saikin, A. M. Alekseev and S. G. Kazarian, *Nano Lett.,* 2017, **17**, 5533–5539.

[8]   Z. X. Wang, X. G. Meng, A. V. Kildishev, A. Boltasseva and V. M. Shalaev, *Laser Photonics Rev.,* 2017, **11**, 1700212.

[9]   O. Hess, J. B. Pendry, S. A. Maier, R. F. Oulton, J. M. Hamm and K. L. Tsakmakidis, *Nat. Mater.,* 2012, **11**, 573–584.

[10]   H. A. Atwater and A. Polman, *Nat. Mater.,* 2010, **9**, 205–213.

[11]   M. Z. Li, U. Guler, Y. A. Li, A. Rea, E. K. Tanyl, Y. Kim, M. A. Noginov, Y. L. Song, A. Boltasseva, V. M. Shalaev and N. A. Kotov, *ACS Energy Lett.,* 2018, **3**, 1578–1583.

[12]   S. Kawata, Y. Inouye and P. Verma, *Nat. Photonics,* 2009, **3**, 388–394.

[13]   W. Cai and V. Shalaev, *Optical Metamaterials: Fundamentals and Applications*, Springer, 2010.

[14]   P. Patsalas, N. Kalfagiannis, S. Kassavetis, G. Abadias, D. V. Bellas, C. Lekka and E. Lidorikis, *Mat. Sci. Eng. R,* 2018, **123**, 1–55.

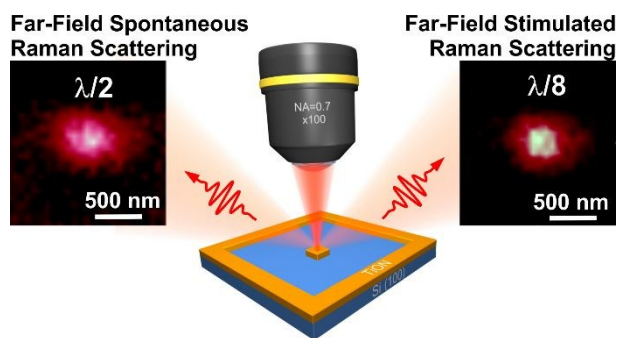[15]   M. Kumar, N. Umezawa, S. Ishii and T. Nagao, *ACS Photonics,* 2016, **3**, 43–50.

[16]   U. Guler, V. M. Shalaev and A. Boltasseva, *Mater. Today,* 2015, **18**, 227–237.

[17]   L. Braic, N. Vasilantonakis, A. Mihai, I. J. V. Garcia, S. Fearn, B. Zou, N. M. Alford,

B. Dolron, R. F. Oulton, S. A. Maier, A. V. Zayats and P. K. Petrov, *ACS Appl. Mater. Inter.,*

2017, **9**, 29857–29862.

[18]   M. Z. Alam, S. A. Schulz, J. Upham, I. De Leon, and R. W. Boyd, *Nat. Photonics*,

2018, **12**, 79–84.

[19] S. Vezzoli, V. Bruno, C. DeVault, T. Roger, V. M. Shalaev, A. Boltasseva, M. Ferrera,

M. Clerici, A. Dubietis and D. Faccio, *Phys. Rev. Lett.*, 2018, **120**, 043902.

[20] Y. U. Lee, E. Garoni, H. Kita, K. Kamada, B. H. Woo, Y. C. Jun, S. M. Chae, H. J. Kim,

K. J. Lee, S. Yoon, E. Choi, F. Mathevet, I. Ozerov, J. C. Ribierre, J. W. Wu and A. D'Aleo,

Adv. Opt. Mater., 2018, **6**, 1701400.

[21] I. Liberal and N. Engheta, *Nat. Photonics*, 2017, **11**, 149–159.

[22] A. Alu and N. Engheta, *Phys. Rev. Lett.*, 2009, **103**, 043902.

[23]   S. A. Maier, *Plasmonics: Fundamentals and Applications*, Springer, 2007.

[24]   M. L. Brongersma, J. W. Hartman and H. A. Atwater, *Phys. Rev. B*, 2000, **62**,

R16356–R16359.

[25]   A. Alu and N. Engheta, *Phys. Rev. B*, 2006, **74**, 205436.

[26]   H. Kim, G. W. Bryant and S. J. Stranick, *Opt. Express,* 2012, **20**, 6042–6051.

[27]   B. Wood, J. B. Pendry and D. P. Tsai, *Phys. Rev. B,* 2006, **74**, 115116.

[28]   J. B. Pendry, *Phys. Rev. Lett.*, 2000, **85**, 3966–3969.

[29]   N. Fang, H. Lee, C. Sun and X. Zhang, *Science*, 2005, **308**, 534–537.

[30]   K. Huang, F. Qin, H. Liu, H. Ye, C. Qiu, M. Hong, B. Luk'yanchuk and J. Teng, *Adv.*

Mater., 2018, **30**, 1704556.

[31]   X. Luo and T. Ishihara, *Appl. Phys. Lett.*, 2004, **84**, 4780–4782.

[32]   X. Luo, *Sci. China Phys. Mech. Astron.*, 2015, **58**, 594201.

[33]   W. S. Cai, D. A. Genov and V. M. Shalaev, *Phys. Rev. B,* 2005, **72**, 193101.

[34]   D. R. Smith, D. C. Vier, T. Koschny and C. M. Soukoulis, *Phys. Rev. E,* 2005, **71**, 036617.

[35]   Z. Szabo, G. H. Park, R. Hedge and E. P. Li, *IEEE T. Microw. Theory,* 2010, **58**, 2646–2653.

[36]   E. Palik, *Handbook of Optical Constants of Solids*, Academic Press, 1985.

[37]   G. V. Naik, J. Kim and A. Boltasseva, *Opt. Mater. Express,* 2011, **1**, 1090–1099.

[38] R. W. Boyd, *Nonlinear Optics*, Academic Press? San Diego, 2008

[39]   S. Schipporeit and D. Mergel, *J. Raman Spectrosc.,* 2018, **49**, 1217–1229.

[40]   T. Mazza, E. Barborini, P. Piseri, P. Milani, D. Cattaneo, A. Li Bassi, C. E. Bottani and C. Ducati, *Phys. Rev. B,* 2007, **75**, 045416.

[41]   T. Ohsaka, F. Izumi and Y. Fujiki, *J. Raman Spectrosc.,* 1978, **7**, 321–234.

[42]   G. A. Tompsett, G. A. Bowmaker, R. P. Cooney, J. B. Metson, K. A. Rodgers and J. M. Seakins, *J. Raman Spectrosc.,* 1995, **26**, 57–62.

[43]   Z. T. Liu, M. D. Thoreson, A. V. Kildishev and V. M. Shalaev, *Appl. Phys. Lett.,* 2009, **95**, 033114.

[44] Giannuzzi L.A., Stevie F.A., *Introduction to Focused Ion Beams: Instrumentation, Theory, Techniques and Practice*: Springer, 2004.

[45]   H. Reddy, U. Guler, Z. Kudyshev, A. V. Kildishev, V. M. Shalaev and A. Boltasseva, *ACS Photonics,* 2017, **4**, 1413–1420.

[46]   Y. Sivan and S. W. Chu, *Nanophotonics,* 2017, **6**, 317–328.

[47]   J. A. Briggs, G. V. Naik, Y. Zhao, T. A. Petach, K. Sahasrabuddhe, D. Goldhaber-Gordon, N. A. Melosh and J. A. Dionne, *Appl. Phys. Lett.,* 2017, **110**, 101901.

[48] S. S. Kharintsev, A. M.Alekseev, J. Loos, *Spectrochim. Acta Part A: Mol. and Biomol. Spectr.,* 2017, **171**, 139–143.

Graphical TOC Entry

Far-Field Spontaneous Raman Scattering
$\lambda/2$
500 nm

Far-Field Stimulated Raman Scattering
$\lambda/8$
500 nm

NA=0.7 x100

Highlight: Beating the diffraction limit in far-field optical imaging becomes possible due to stimulated Raman scattering in percolated metal-dielectric nanocomposites.

Nanoscale Accepted Manuscript